

THE ABSOLUTE CALIBRATION OF THE EUV IMAGING SPECTROMETER ON *HINODE*

HARRY P. WARREN¹, IGNACIO UGARTE-URRA², AND ENRICO LANDI³

¹Space Science Division, Naval Research Laboratory, Washington, DC 20375 USA

²College of Science, George Mason University, 4400 University Drive, Fairfax, VA 22030 USA and

³Department of Atmospheric, Oceanic and Space Sciences, University of Michigan, Ann Arbor, MI 48109, USA

Draft version March 1, 2018

ABSTRACT

We investigate the absolute calibration of the EUV Imaging Spectrometer (EIS) on *Hinode* by comparing EIS full-disk mosaics with irradiance observations from the EUV Variability Experiment (EVE) on the *Solar Dynamics Observatory*. We also use ultra-deep ($> 10^5$ s) exposures of the quiet corona above the limb combined with a simple differential emission measure model to establish new effective area curves that incorporate information from the most recent atomic physics calculations. We find that changes to the EIS instrument sensitivity are a complex function of both time and wavelength. We find that the sensitivity is decaying exponentially with time and that the decay constants vary with wavelength. The EIS short wavelength channel shows significantly longer decay times than the long wavelength channel.

Subject headings: Sun: corona

1. INTRODUCTION

Understanding the physical properties of the solar corona is largely dependent on plasma diagnostics derived from spectroscopic observations. The utility of most plasma diagnostics is directly related to our understanding of both the underlying atomic physics and the radiometric calibration of the instrument used to observe them. Unfortunately, establishing and maintaining the calibration of satellite borne instruments has proven to be challenging, particularly at extreme ultraviolet (EUV, 50–1200 Å) wavelengths where many spectroscopically interesting emission lines lie.

In this paper we investigate the interplay between the absolute calibration of the EUV Imaging Spectrometer (EIS Culhane et al. 2007) on the *Hinode* mission and our ability to measure the properties of the solar corona. Information on the absolute calibration can be summarized in the “effective area,” which combines the geometrical size and efficiency of the various components along the optical path of an instrument. EIS observes in two EUV wavelength ranges (171–212 Å and 245–291 Å) which contain many emission lines that can be used to determine the temperature and density structure of the corona. Such measurements are critical for constraining theories of coronal heating. The observation of temperature and density insensitive emission lines can also be used to evaluate the relative calibration of EIS. As we describe here, detailed analysis shows that the pre-flight calibration is inconsistent with a number of established line ratios. These line ratios also indicate that the relative calibration has been changing with time.

The EIS pre-flight calibration and its evolution early in the mission was studied by Wang et al. (2011), who compared EIS observations with simultaneous measurements from the EUNIS sounding rocket experiment flown on 2007 November 6. For these observations the ratio of EUNIS to EIS intensity was found to be approximately constant as a function of wavelength, suggesting that the shape of the EIS pre-flight effective areas were accurate. The mean intensity ratio was 1.22, indicating a decrease in response of about 20% since launch. This corresponds to a decay constant of about 5.6 years.

The long-term evolution of the EIS sensitivity was inves-

tigated by Mariska (2013), who measured the intensity of several emission lines observed in the quiet Sun from late 2006 to early 2012. He found that the absolute intensities for Fe VIII 185.213 Å and Si VII 275.352 Å decayed with a time constant of about 20 years during the first 6 years of the mission, suggesting that the calibration was very stable. This analysis is predicated on the assumption that intensities measured in the quiet Sun are relatively constant over time. Intensities in He II 256.317 Å showed a much more rapid decline, but this line is blended with coronal emission and Mariska (2013) concluded that the evolution of these intensities over time was influenced by solar cycle effects.

Del Zanna (2013) noted that there were several line ratios observed with EIS that did not agree with previous observations or atomic calculations. The Fe XIV 274.203 Å to 211.316 Å ratio, for example, is largely insensitive to variations in temperature and density. The ratio observed with EIS not only disagreed with theory but changed with time, suggesting that time-dependent modifications to the pre-flight calibration were needed. Through the systematic analysis of various line ratios Del Zanna (2013) provided revised effective area curves for both EIS channels. Del Zanna (2013) concluded that the degradation was primarily in the long wavelength channel and that the effective area in the short wavelength channel remains constant in time.

There are, however, several limitations to using line ratios for calibration purposes. They establish the relative but not the absolute calibration. Also, the changes to the calibration suggested by line ratios may not be unique. There is no way to know how to distribute modifications to the effective areas without additional information. Furthermore, many of the lines used in such an analysis are weak and are difficult to measure. Modifications to the calibration based on weak lines may lead to problems with the intensities of the strong lines that are more generally used for analysis.

Here we extend the previous work on the EIS calibration in two ways. First, we compare full-disk mosaics constructed by scanning the EIS slot over the Sun with irradiance observation made by the EUV Variability Experiment (EVE Woods et al. 2012) on the *SDO* mission. These comparisons pro-

vide a means of establishing the absolute calibration for EIS. Second, we combine ultra-deep EIS observations from above the limb in the quiet Sun with a simple temperature model to simultaneously determine the differential emission measure distribution and the time-dependent changes to the effective areas which best fit all of the available spectral lines. This analysis takes advantage of the fact that the quiet corona generally has a very narrow temperature distribution (e.g., Raymond et al. 1997; Feldman et al. 1998; Landi et al. 2002; Warren & Brooks 2009).

2. COMPARISONS WITH EVE

EIS has been optimized to provide observations at relatively high spatial and spectral resolution (see Korendyke et al. 2006 for details). However, in addition to the narrow 1'' and 2'' slits EIS also can observe with a 40'' wide slot. These slot observations are similar to those obtained from the SO2-A instrument on *Skylab* (Tousey et al. 1977). The 40'' width of the EIS slot, however, yields images which integrate over only about 1 Å of the solar spectrum. This limits the amount of overlap between spectral features. To build up a larger field of view the slot is stepped across the Sun and a short exposure is taken at each position. By re-pointing the spacecraft a number of times a nearly complete scan of the Sun is possible within a few hours of observing.

In June of 2009 EIS began executing a full-disk scan of the Sun approximately once every three weeks. Observations are taken in Fe X 180.401 Å, Fe XII 195.119 Å, Fe XIII 202.044 and 203.826 Å, He II 256.317 Å, Fe XVI 262.984 Å, Si VII 275.368, and Fe XV 284.160 Å. Beginning on 2013 March 19 Fe XIV 211.316 Å and 274.203 Å, Si X 258.375 Å, and Si X 264.233 Å were added to the observing program.

Each of these observations has been processed to remove the CCD pedestal, dark current, and spikes from warm and hot pixels. These data are also calibrated using the pre-flight effective areas. The spatially resolved intensity (or radiance) measured on the Sun is related to the irradiance measured at earth by

$$F(\lambda) = \frac{a}{R^2} \sum_{i=1}^N I_i(\lambda), \quad (1)$$

where a is the area on the Sun imaged in a detector pixel, R is the earth-Sun distance, and N is the number of EIS pixels in the full-disk mosaic. Because the EIS mosaic requires several hours to obtain and the *Hinode* spacecraft pointing often drifts over time, each raster is cross-correlated with either an EIT 195 Å (Delaboudinière et al. 1995) or an AIA 193 Å (Lemen et al. 2012) image to correct for this. Several example EIS full-disk mosaics are shown in Figure 1. Note that each mosaic covers only a finite portion of the corona above the limb. Based on comparisons with EIT and AIA images we estimate that EIS underestimates the irradiance by a few percent. Some EIS images have gaps due to data dropouts and data with more than 2.5% missing pixels are not used for our analysis.

For each full-disk mosaic we compare the irradiance inferred from EIS with the corresponding irradiance measured by EVE. EVE provides absolutely calibrated, spatially unresolved measurements of the spectral irradiance at a resolution of about 1 Å. The absolute calibration of EVE is monitored using redundant channels and rocket underflights (Hock et al. 2012). For comparison with EIS we read the version 3 daily

TABLE 1
EIS TO EVE IRRADIANCE RATIOS^a

| Line | EIS/EVE | τ | Comment |
|-----------------|---------|--------|---------|
| Fe XI 180.401 | 0.63 | 20.6 | |
| Fe VIII 185.213 | 0.54 | — | Blended |
| Fe XII 195.119 | 1.00 | 14.3 | |
| Fe XIII 202.044 | 1.27 | 18.7 | |
| Fe XIII 203.826 | 1.42 | 24.8 | Blended |
| Fe XIV 211.316 | 1.52 | — | |
| He II 256.317 | 0.49 | 10.3 | Blended |
| Si X 258.375 | 0.36 | — | Blended |
| Fe XVI 262.984 | 0.36 | 10.8 | |
| S X 264.233 | 0.34 | — | Blended |
| Fe XIV 274.203 | 0.54 | — | |
| Si VII 275.368 | 0.40 | 4.8 | Blended |
| Fe XV 284.160 | 0.72 | 11.0 | |

^a The EIS/EVE ratio is the median ratio from the beginning of the *SDO* mission to 2013 May 1. τ is the time constant in years derived from an exponential fit to the EIS/EVE ratio. Some EIS lines have been observed only very recently in the full-disk mosaics and time constants are not yet available.

merged EVE data, convert the spectrum to cgs units, and integrate over a 1 Å bandpass centered on the line of interest. The ratio of EIS to EVE irradiances as a function of time for Fe XII 195.119 Å is shown in Figure 1. This comparison suggests that the EIS calibration is changing very slowly over time, generally consistent with the results of Mariska (2013), although the time constant we measure is 14.5 years instead of 20.2 years. This comparison also suggests that while EIS and EVE agree on an absolute scale during most of the period from 2010 through 2013, the absolute calibration of EIS at this wavelength is unlikely to have been correct at launch.

Inspection of the EIS to EVE ratios at the other wavelengths suggests that both the absolute and relative calibration differs from the pre-flight measurements. A summary of the median EIS/EVE ratios observed from the beginning of the *SDO* mission to 2013 May 1 are given in Table 1. In the long wavelength channel the EIS irradiances are generally below those measured by EVE and show a much more rapid decay (approximately 9 to 12 years). In the short wavelength channel the EIS to EVE ratio varies from below 1 at the shortest wavelengths to approximately 1.5 at the longest wavelengths. The time constants are also systematically larger in the short wavelength channel, ranging from 15 to 27 years. We note that at several of these wavelengths there is significant blending in the EVE spectra as well as significant overlap in the EIS slot images. This complicates the interpretation of the ratios for these lines.

As we will discuss in detail later in the paper, the complex behavior in the effective areas as a function of wavelength and time is broadly consistent with the results of Del Zanna (2013). To fully characterize the EIS calibration, however, more detailed analysis is required. In the next section we will combine very deep EIS exposures above the limb with a simple temperature model to infer the best-fit effective areas as a function of time.

3. QUIET SUN EMISSION MEASURE

Many previous studies have indicated that the distribution of temperatures above the limb is very narrow (e.g., Raymond et al. 1997; Feldman et al. 1998; Landi et al. 2002; Warren & Brooks 2009). These results suggest that a single Gaussian is a good representation for the differential emission measure,

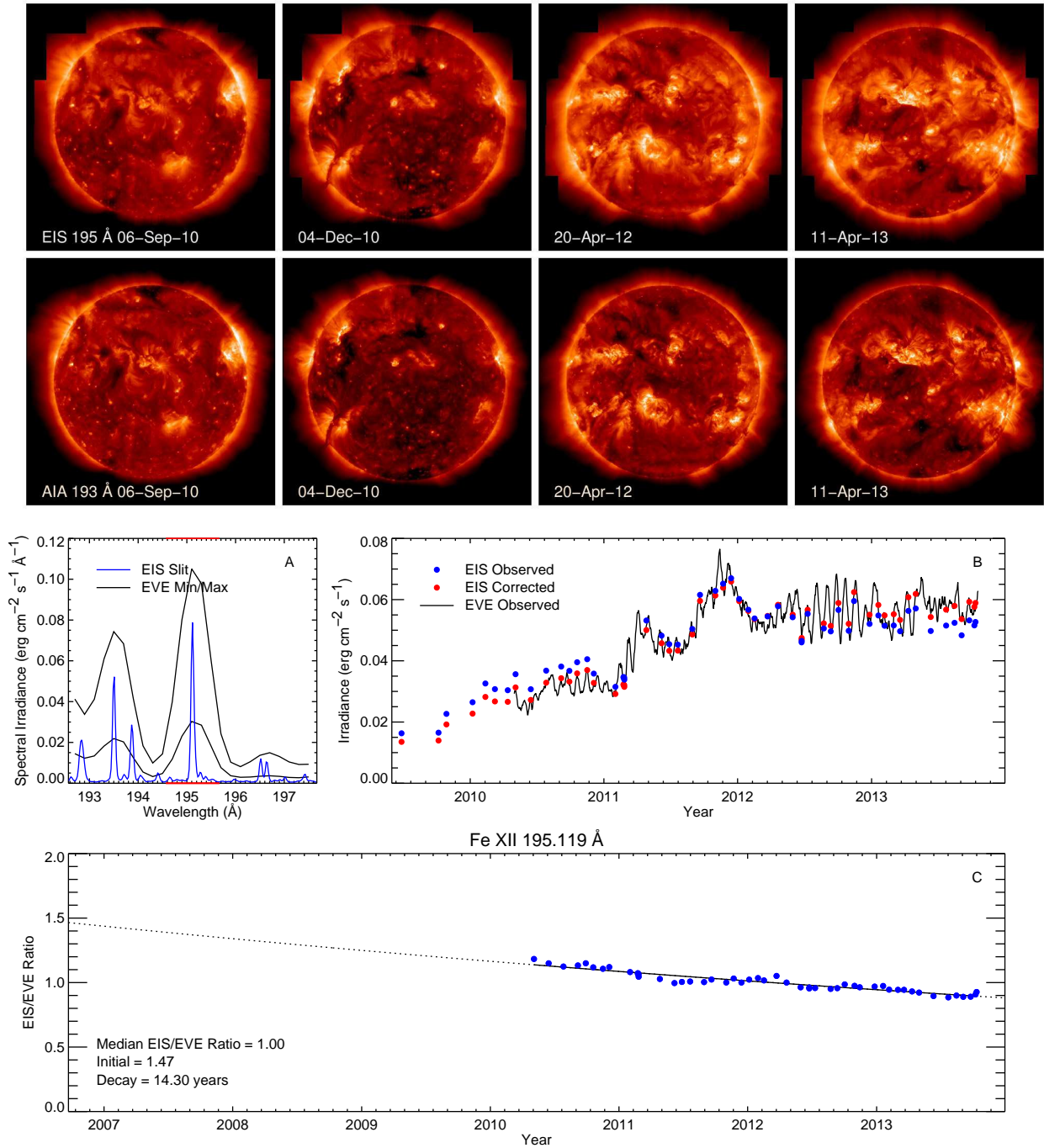


FIG. 1.— A comparison of irradiances in the Fe XII 195 Å emission line measured with EIS and EVE. The top two rows show representative EIS full-disk mosaics constructed by rastering the 40'' slot as well as AIA 193 Å images taken the same day. Panel A shows EVE spectral irradiances during periods of low and high solar activity. For reference we also show a high spectral resolution EIS spectrum from an active region. This spectrum is scaled arbitrarily. Panel B shows the EVE and EIS irradiances as a function of time. Panel C shows the ratio of EIS to EVE during the SDO mission. The solid line is an exponential fit to the observed ratio. The dotted line is an extrapolation of the fit to earlier and later times. EIS irradiances corrected for the observed decay are also shown in Panel B.

which we write as

$$\xi(T) = \frac{EM_0}{\sigma_T \sqrt{2\pi}} \exp \left[-\frac{(T - T_0)^2}{2\sigma_T^2} \right]. \quad (2)$$

We can convolve the differential emission measure with the plasma emissivity for an emission line to compute the line

intensity using

$$I_\lambda = \frac{1}{4\pi} \int \epsilon_\lambda(n_e, T) \xi(T) dT. \quad (3)$$

Here the plasma emissivity is the radiated power (erg s⁻¹) divided by the square of the electron number density, n_e . For this work we use version 7.1 of the CHIANTI atomic physics

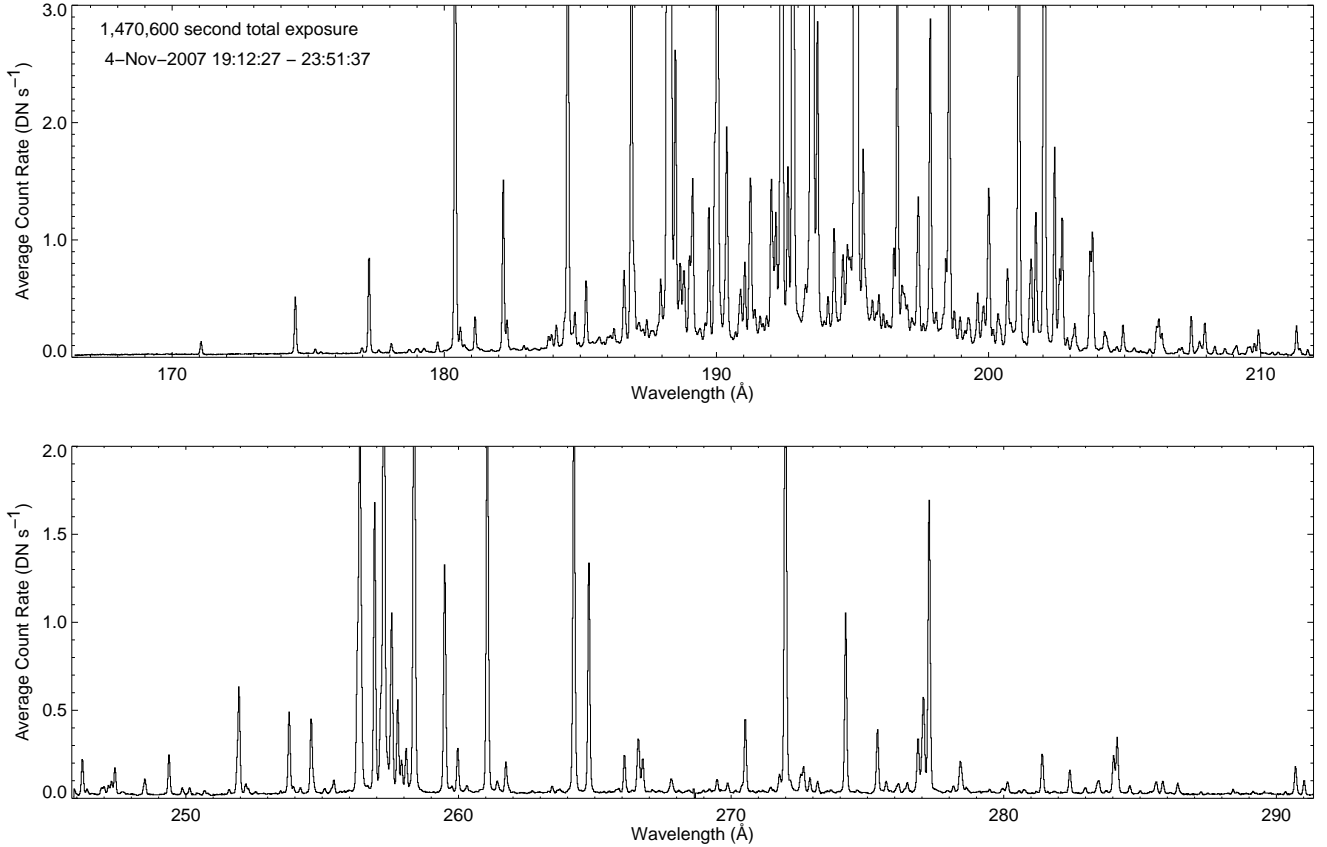


FIG. 2.— An ultra-deep spectrum of the quiet Sun above the limb constructed by averaging 38 300 s exposures and 129 pixels along the slit for an effective exposure time of 1,470,600 s. The scale in the Y direction has been cutoff to emphasize the weak lines. The peak count rates are approximately 50 DN s^{-1} .

database (e.g., Dere et al. 1997; Landi et al. 2013) to compute the plasma emissivities. To facilitate rapid calculations we have pre-computed grids of emissivities as a function of temperature and density. We assume the CHIANTI ionization equilibria and the coronal abundances of Feldman (1992). Since many of the Fe emission lines observed at these wavelengths have some density sensitivity, we leave the density as a free-parameter to be determined through the fitting process and we do not exclude density sensitive lines from our analysis.

For a given intensity the number of photons that are detected in a pixel on the CCD is equal to

$$N_{\text{photons}} = \frac{a}{R^2} I_{\lambda} A(\lambda) t, \quad (4)$$

where a is the area of the Sun imaged in a pixel and R is the earth-Sun distance, I_{λ} is the intensity at the surface of the Sun in units of $\text{photon cm}^{-2} \text{ s}^{-1} \text{ sr}^{-1}$, $A(\lambda)$ is the effective area, and t the exposure time. The effective area includes information on the collecting area of the mirrors and the efficiency of the various optical elements, filters, and the detectors (Lang et al. 2006). The photons that strike the CCD generate electrons that are read out by the detector electronics. The number of electrons is equal to

$$N_e = N_{\text{photons}} \frac{hc}{\lambda} \frac{1}{3.65 \text{ eV}}. \quad (5)$$

Finally, the detector electronics divide the number of electrons recorded by a gain factor to produce a “data number” value

that is sent to the ground in the telemetry stream

$$\text{DN} = N_e / G. \quad (6)$$

For EIS the gain is set at 6.3.

For most differential emission measure calculations with EIS the pre-flight effective areas from Lang et al. (2006) have been used. Here we have the more ambitious goal of using the observations to solve for both the best-fit differential emission measure parameters $\{EM_0, \sigma_T, T_0, n_e\}$ and effective areas simultaneously. To model the variation in the effective area we introduce a series of equally spaced spline knots that are used to interpolate the effective areas as a function of wavelength. The parameter to be optimized in the calculation is the ratio of the corrected to pre-flight effective area $\{r_k(\lambda_k, t)\}$.

For this work we assume 7 knots for each EIS wavelength range. With a total of 14 knots and 4 DEM variables there are many free parameters in the model. While it is easy to include enough emission lines to make the problem well posed, it is important to consider both the temperature of formation as well as the wavelength for each line. Lines from many different ionization stages are needed to constrain the DEM while multiple emission lines at each wavelength are needed to constrain the determination of the effective areas.

Measuring emission from lines that span the temperature range of the quiet corona is relatively easy. Emission from lines of Fe VIII to Fe XVI are often present above the limb. The challenge for our approach is measuring emission lines over the complete wavelength range of each detector. This is difficult at the ends of the detectors where the effective areas

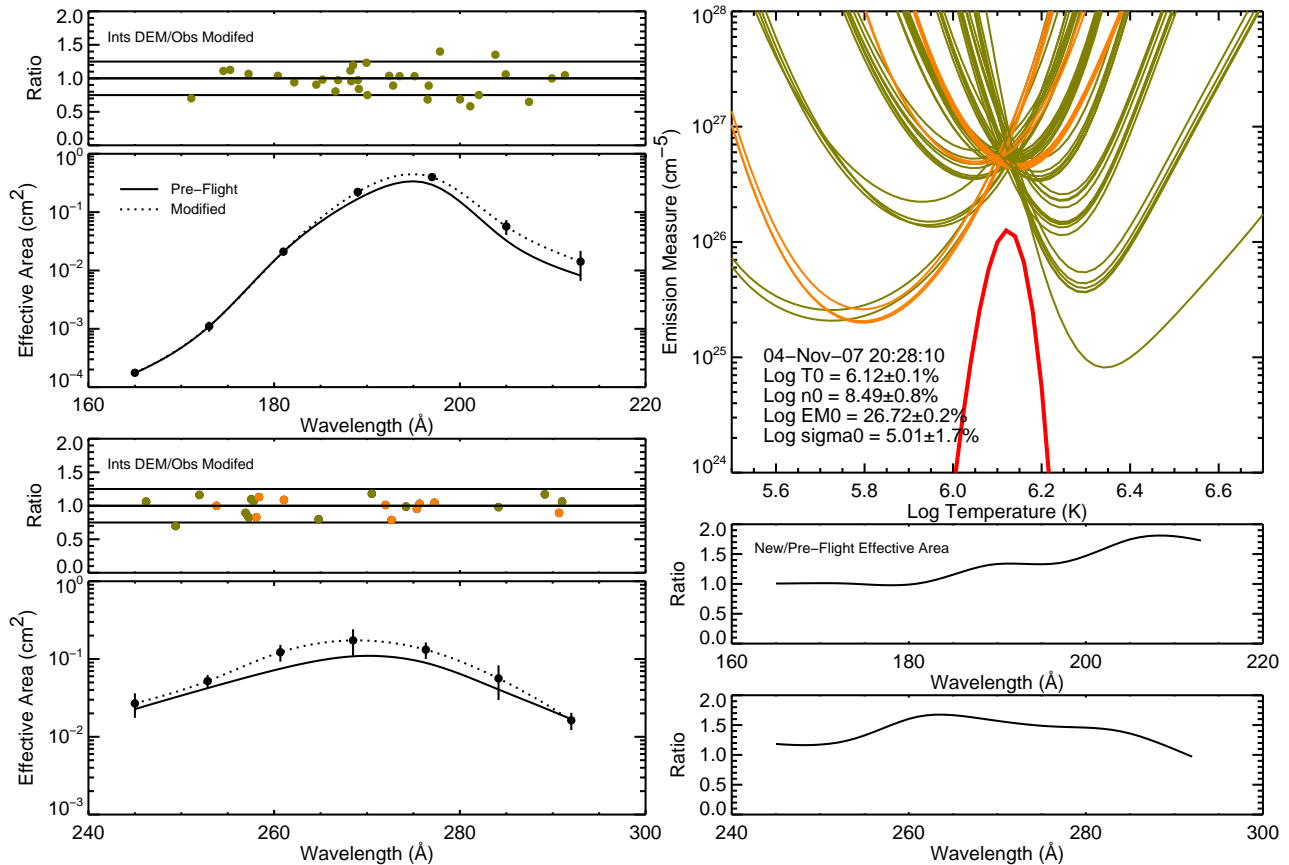


FIG. 3.— Simultaneous optimization of the differential emission measure and effective areas for the spectrum shown in Figure 2. The left panels show the pre-flight and corrected effective areas as a function of wavelength for both EIS detectors. The left panels also show the ratio of the observed intensities using the corrected effective areas. The panels on the lower right show the ratio of the corrected to the pre-flight effective areas. The panel on the upper right shows the best-fit differential emission measure distribution and EM-loci curves for each line. In these plots green corresponds to Fe lines and orange to Si lines.

are very small and count rates are generally low. To overcome this we have made use of full CCD rasters with very long exposure times taken by EIS in the quiet Sun above the limb. The EIS study `EL_FULL_CCD_W_SUMER`, which takes 7 300 s exposures over a narrow $14'' \times 512''$ area, is particularly useful for this application. We have processed the data for each of these observations using `eis_prep` to remove dark current and hot pixels from the detector exposures. We do not apply the calibration at this stage and leave the observations in units of data number (DN). We then select an area along the slit and compute the distribution of DN at each wavelength. We use the median and standard deviation to characterize the intensity and the uncertainty in the intensity at each wavelength. Using the median, as opposed to the average, helps limit the impact of residual “warm pixels” on the intensity. Some pixels on the EIS detector produce very high count rates even for exposures taken with the shutter closed. These “hot pixels” are easily identified in dark exposures. Other pixels produce slightly elevated levels of signal during dark exposures and are more difficult to identify.

In Figure 2 we show the average spectrum from an observation of 7 consecutive runs of `EL_FULL_CCD_W_SUMER`. The observations began on 2007 November 4 19:12 and ended at on the same date at 23:51 UT. The EIS field of view was centered at $(990'', -50'')$ about $22''$ above the limb of the Sun. The central 129 pixels along the slit have been averaged over 38 exposures (11 exposures were corrupted in transmission to the ground) for a total of 4,902 intensity measurements at each

wavelength. Since each exposure is 300 s the spectrum represents 1,470,600 s of effective exposure time and allows weak lines at the ends of the detector to be measured.

Using the average spectrum we compute intensities for each emission line of interest by fitting the profile with a Gaussian and a linear background. For lines that are close in wavelength multiple Gaussians are fit simultaneously. For this work we focus on emission lines from Fe and Si to minimize abundance effects. At this stage the intensities are converted from DN to physical units using the pre-flight effective areas and equations 4–6.

Equations 3 and 4 show that the observed count rate is proportional to the product of the effective area and the emission measure. This means we cannot solve our system of equations without additional constraints. Our primary assumption is that the EIS effective area near 195 \AA follows the decay derived from the EIS/EVE comparisons that is shown in Figure 1. Since observations with the AIA 193 \AA channel are generally consistent with the absolutely calibrated EVE measurements at the same wavelength (Boerner et al. 2013), this assumption helps insure that any combined EIS-AIA-EVE analysis uses a consistent inter-calibration.

We further assume that the trend measured during the *SDO* mission can be extrapolated back to the launch of *Hinode*. While this assumption should be regarded with considerable skepticism, it is consistent with the simple exponential decays measured by Mariska (2013) from launch to mid 2012.

Unfortunately there is only a single EIS line near both 171

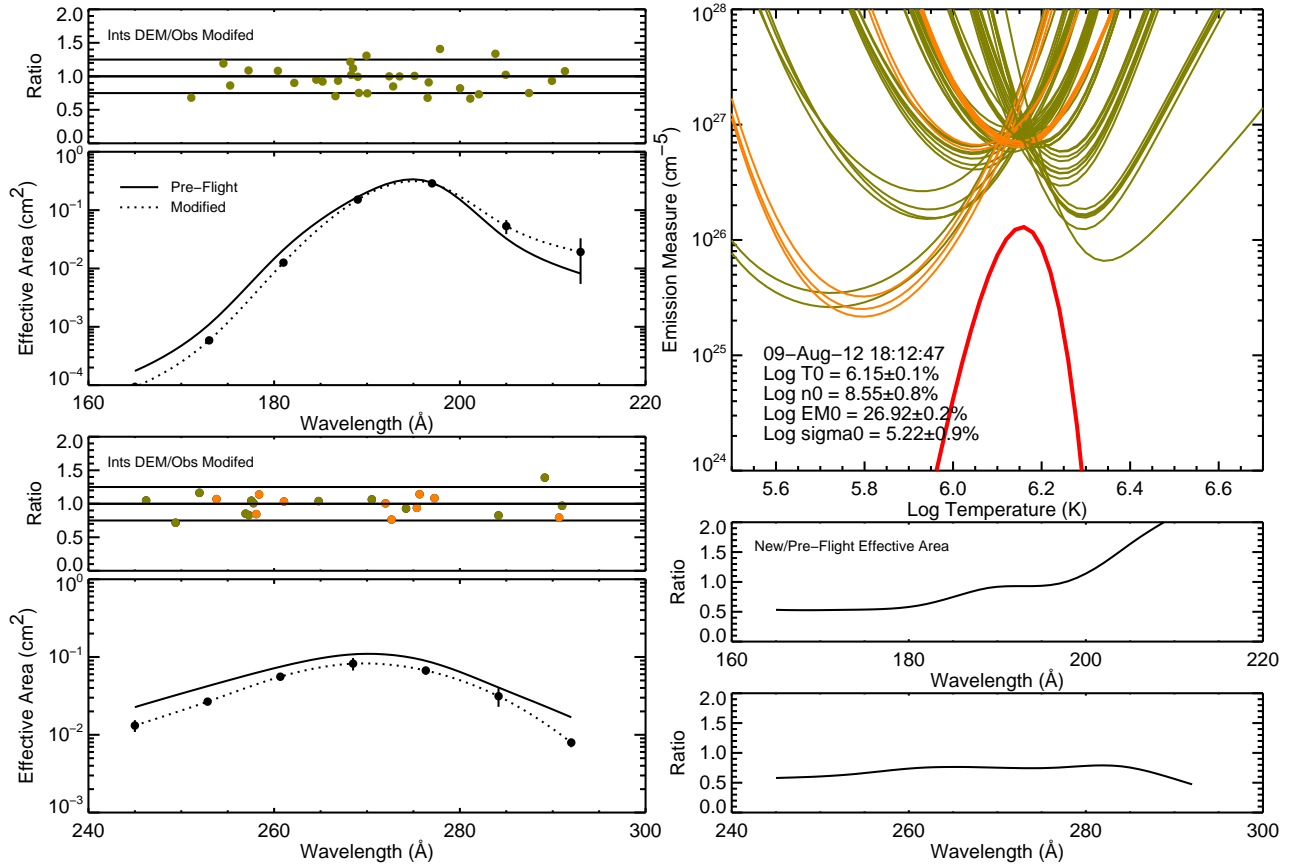


FIG. 4.— The same as Figure 3 but for observations taken later in the mission. The effective area in the long wavelength channel is about a factor of 2 lower than the pre-flight value.

and 284 \AA so we introduce an additional constraint that the ratio of the corrected to pre-flight effective area is the same as it is at the next wavelength. That is, we assume that $r_k = r_{k+1}$ for the first knot in the short wavelength band.

Finally, with the very long exposure times for these observations Fe XII 193.509 and 195.119 \AA are often saturated. We replace any measured intensities for these lines with intensities inferred from the intensity of Fe XII 192.394 \AA and the ratios from CHIANTI of 2.1 and 3.1, respectively.

With these constraints we use the MPFIT package (Markwardt 2009) for implementing Levenberg-Marquardt least-squares minimization. We use $\{10^{27}, 10^{5.5}, 10^{6.2}, 10^9\}$ as initial conditions for the emission measure parameters and, except for the knot closest to 195 \AA , we assume $r_k = 1$ for the initial effective area ratios. The value for the knot closest to 195 \AA is fixed to the value of the EIS/EVE ratio shown in Figure 1. At each iteration new intensities are computed from the emission measure and effective area ratio parameters. Iteration continues until the differences between the computed and observed intensities reaches a minimum. In Figure 3 we show the solution for the 2007 November 4 spectrum discussed earlier. A summary of the intensities is given in Table 2. For this date the EIS/EVE decay curve indicates that the effective area at 195 \AA is 1.35 times the pre-flight value. The best-fit solution indicates that the effective areas need to be raised at wavelengths above 195 \AA as well as in the central region of the long wavelength detector.

For comparison we have also run this calculation with the effective area ratios fixed at unity so that the pre-flight calibra-

tion is used in computing the DEM. The parameters derived for the DEM are very similar to those computed with the corrected effective area curves, but now systematic trends in the calculated intensities are evident. The computed intensities for lines at wavelengths above 195 \AA and near 260 \AA are generally too small while the intensities at 180 \AA and below are generally too large.

The application of this analysis to the 2007 November 4 data yields new effective areas curves for one time. In Figure 4 we show the analysis for off-limb observations taken 2012 August 9, almost 5 years after the data shown in Figure 3. The resulting effective areas curves are similar in shape to those calculated for the earlier data, but the magnitude has diminished at many wavelengths.

There are, unfortunately, only a few observations taken above the limb in the quiet corona which have the required signal to noise for this analysis. We have only been able to perform the DEM calculations for a total 5 data sets, two of which were taken the same day. In Figure 5 we plot our effective area as a function of time for several selected wavelengths. Also shown are exponential fits of the form

$$A_{\text{corrected}}(\lambda, t) = A_{\text{corrected}}(\lambda, t_0) \exp\left[-\frac{t - t_0}{\tau(\lambda)}\right], \quad (7)$$

where t_0 is chosen to be 2006 September 22, the *Hinode* launch date, and $\tau(\lambda)$ is the wavelength dependent time constant. An exponential model is consistent with time evolution of the sensitivity found by Mariska (2013). The decay in the sensitivity of the long wavelength channel is fairly uniform,

TABLE 2
 INTENSITIES MEASURED IN THE QUIET CORONA ABOVE THE LIMB 2007 NOVEMBER 4 WITH EIS^a

| Line | Intensity | | | | | | | <i>R</i> |
|-----------------|-------------|------------------|-------------------|----------|------------------|----------|------------|----------|
| | <i>DN/s</i> | <i>photons/s</i> | <i>pre-flight</i> | σ | <i>corrected</i> | σ | <i>DEM</i> | |
| Fe IX 171.073 | 0.37 | 0.12 | 1110.50 ± | 254.98 | 1096.75 ± | 251.82 | 769.41 | 1.43 |
| Fe X 174.532 | 1.72 | 0.56 | 839.70 ± | 185.35 | 842.92 ± | 186.06 | 935.89 | 0.90 |
| Fe X 175.263 | 0.13 | 0.04 | 50.64 ± | 14.80 | 51.12 ± | 14.95 | 57.57 | 0.89 |
| Fe X 177.239 | 2.93 | 0.96 | 473.10 ± | 104.28 | 483.36 ± | 106.54 | 515.45 | 0.94 |
| Fe XI 180.401 | 18.25 | 6.11 | 845.41 ± | 186.07 | 850.53 ± | 187.20 | 882.36 | 0.96 |
| Fe XI 182.167 | 5.23 | 1.77 | 130.93 ± | 28.83 | 126.22 ± | 27.80 | 118.64 | 1.06 |
| Fe X 184.536 | 20.61 | 7.05 | 246.86 ± | 54.34 | 217.93 ± | 47.98 | 197.35 | 1.10 |
| Fe VIII 185.213 | 2.10 | 0.72 | 21.03 ± | 4.64 | 18.06 ± | 3.99 | 17.71 | 1.02 |
| Fe VIII 186.601 | 2.54 | 0.88 | 18.41 ± | 4.06 | 14.98 ± | 3.31 | 12.06 | 1.24 |
| Fe XII 186.880 | 13.81 | 4.79 | 94.34 ± | 20.77 | 76.01 ± | 16.73 | 73.97 | 1.03 |
| Fe XI 188.216 | 92.24 | 32.20 | 488.42 ± | 107.48 | 377.58 ± | 83.09 | 421.00 | 0.90 |
| Fe XI 188.299 | 64.98 | 22.69 | 339.18 ± | 74.64 | 261.65 ± | 57.58 | 250.45 | 1.04 |
| Fe IX 188.497 | 8.75 | 3.06 | 44.17 ± | 9.72 | 33.91 ± | 7.46 | 40.49 | 0.84 |
| Fe XI 189.017 | 2.78 | 0.97 | 12.91 ± | 2.84 | 9.81 ± | 2.16 | 9.55 | 1.03 |
| Fe XI 189.123 | 5.39 | 1.89 | 24.63 ± | 5.42 | 18.67 ± | 4.11 | 15.71 | 1.19 |
| Fe IX 189.941 | 6.03 | 2.13 | 24.48 ± | 5.39 | 18.36 ± | 4.04 | 22.62 | 0.81 |
| Fe X 190.038 | 24.64 | 8.68 | 98.63 ± | 21.71 | 73.93 ± | 16.27 | 55.48 | 1.33 |
| Fe XII 192.394 | 65.10 | 23.23 | 199.53 ± | 43.91 | 149.07 ± | 32.81 | 154.64 | 0.96 |
| Fe XI 192.813 | 43.46 | 15.54 | 128.50 ± | 28.28 | 96.14 ± | 21.16 | 85.79 | 1.12 |
| Fe XII 193.509 | 149.48 | 53.65 | 419.01 ± | 92.21 | 314.32 ± | 69.17 | 324.68 | 0.97 |
| Fe XII 195.119 | 238.89 | 86.45 | 618.54 ± | 136.14 | 465.15 ± | 102.38 | 479.81 | 0.97 |
| Fe XIII 196.525 | 2.54 | 0.92 | 6.57 ± | 1.45 | 4.90 ± | 1.08 | 3.35 | 1.46 |
| Fe XII 196.640 | 11.43 | 4.17 | 29.73 ± | 6.54 | 22.13 ± | 4.87 | 19.71 | 1.12 |
| Fe IX 197.862 | 10.15 | 3.72 | 29.00 ± | 6.39 | 21.10 ± | 4.65 | 29.54 | 0.71 |
| Fe XIII 200.021 | 5.80 | 2.15 | 26.21 ± | 5.77 | 17.82 ± | 3.93 | 12.22 | 1.46 |
| Fe XIII 201.121 | 16.18 | 6.04 | 106.92 ± | 23.53 | 69.76 ± | 15.35 | 40.65 | 1.72 |
| Fe XIII 202.044 | 35.26 | 13.21 | 335.62 ± | 73.87 | 211.35 ± | 46.52 | 158.66 | 1.33 |
| Fe XIII 203.826 | 3.96 | 1.50 | 71.01 ± | 15.66 | 41.98 ± | 9.26 | 56.75 | 0.74 |
| Fe XIII 204.937 | 0.87 | 0.33 | 20.60 ± | 4.56 | 11.81 ± | 2.62 | 12.51 | 0.94 |
| Fe X 207.449 | 1.19 | 0.46 | 44.75 ± | 9.91 | 24.76 ± | 5.49 | 16.07 | 1.54 |
| Fe XIII 209.916 | 0.72 | 0.28 | 42.58 ± | 9.48 | 23.65 ± | 5.27 | 23.61 | 1.00 |
| Fe XIV 211.316 | 0.82 | 0.32 | 60.79 ± | 13.53 | 34.27 ± | 7.63 | 35.85 | 0.96 |
| Fe XIII 246.208 | 0.81 | 0.37 | 25.72 ± | 5.71 | 21.95 ± | 4.87 | 23.30 | 0.94 |
| Fe XII 249.388 | 0.83 | 0.38 | 21.53 ± | 4.79 | 18.45 ± | 4.11 | 12.87 | 1.43 |
| Fe XIII 251.953 | 2.30 | 1.08 | 46.44 ± | 10.26 | 38.51 ± | 8.51 | 44.72 | 0.86 |
| Si X 253.791 | 1.87 | 0.88 | 31.99 ± | 7.05 | 25.21 ± | 5.56 | 25.20 | 1.00 |
| Fe XI 256.925 | 6.15 | 2.93 | 82.44 ± | 18.15 | 57.44 ± | 12.65 | 51.31 | 1.12 |
| Fe X 257.262 | 15.59 | 7.44 | 204.15 ± | 44.95 | 140.28 ± | 30.89 | 115.84 | 1.21 |
| Fe XI 257.547 | 4.18 | 2.00 | 53.66 ± | 11.81 | 36.45 ± | 8.03 | 40.01 | 0.91 |
| Fe XI 257.772 | 1.85 | 0.88 | 23.35 ± | 5.15 | 15.72 ± | 3.47 | 16.77 | 0.94 |
| Si IX 258.073 | 0.81 | 0.39 | 9.97 ± | 2.22 | 6.63 ± | 1.47 | 5.50 | 1.21 |
| Si X 258.375 | 14.18 | 6.79 | 171.97 ± | 37.85 | 113.13 ± | 24.90 | 127.88 | 0.88 |
| Si X 261.058 | 10.05 | 4.87 | 102.61 ± | 22.58 | 62.49 ± | 13.75 | 68.00 | 0.92 |
| Fe XIV 264.787 | 3.59 | 1.77 | 29.82 ± | 6.57 | 17.88 ± | 3.94 | 14.27 | 1.25 |
| Fe XIV 270.519 | 1.70 | 0.85 | 12.02 ± | 2.65 | 7.71 ± | 1.70 | 9.10 | 0.85 |
| Si X 271.990 | 12.12 | 6.11 | 86.83 ± | 19.10 | 56.66 ± | 12.47 | 57.31 | 0.99 |
| Si VII 272.641 | 0.59 | 0.30 | 4.32 ± | 0.97 | 2.84 ± | 0.63 | 2.24 | 1.27 |
| Fe XIV 274.203 | 3.99 | 2.03 | 30.77 ± | 6.77 | 20.54 ± | 4.52 | 20.27 | 1.01 |
| Si VII 275.368 | 1.47 | 0.75 | 12.08 ± | 2.66 | 8.14 ± | 1.80 | 7.77 | 1.05 |
| Si VII 275.665 | 0.22 | 0.11 | 1.84 ± | 0.42 | 1.24 ± | 0.28 | 1.28 | 0.97 |
| Si X 277.265 | 6.99 | 3.60 | 66.13 ± | 14.55 | 44.99 ± | 9.90 | 47.06 | 0.96 |
| Fe XV 284.160 | 1.29 | 0.68 | 24.87 ± | 5.50 | 17.92 ± | 3.96 | 17.56 | 1.02 |
| Fe XIV 289.151 | 0.05 | 0.03 | 1.67 ± | 0.81 | 1.46 ± | 0.71 | 1.71 | 0.85 |
| Si IX 290.687 | 0.67 | 0.36 | 26.92 ± | 6.03 | 25.60 ± | 5.74 | 22.87 | 1.12 |
| Fe XII 291.010 | 0.32 | 0.17 | 13.40 ± | 3.10 | 12.99 ± | 3.00 | 13.81 | 0.94 |

^a The intensities computed from the pre-flight and corrected effective areas as well as the intensity computed from the DEM are in units of $\text{erg cm}^{-2} \text{s}^{-1} \text{sr}^{-1}$ the other intensities are in units of data number per second and detected photons per second. *R* is the ratio of corrected to DEM calculated intensity.

with $\tau \approx 6\text{--}7$ years. The decay in the sensitivity of the short wavelength channel is slower and less uniform, with $\tau \approx 9$ years at the shortest wavelengths and a slight increase of sensitivity at the end of the short wavelength detector.

Our analysis is generally consistent with the results of Del Zanna (2013). Both sets of corrections indicate a reduction of the EIS effective area at the shortest wavelengths in the short wavelength channel as well as a relative increase near the central part of the long wavelength detector (see Figure 8 from Del Zanna 2013). Our analysis, however, also suggests

a relative increase in the effective area at the longest wavelengths in the short wavelength detector. Our comparisons with EVE indicate a slow decrease in the sensitivity of the short wavelength detector, which we have incorporated into our analysis. Using observation of the transition region intensities taken in the quiet Sun, Del Zanna 2013 concluded that sensitivity in the short wavelength detector has remained approximately constant during the mission.

4. COMPARISONS

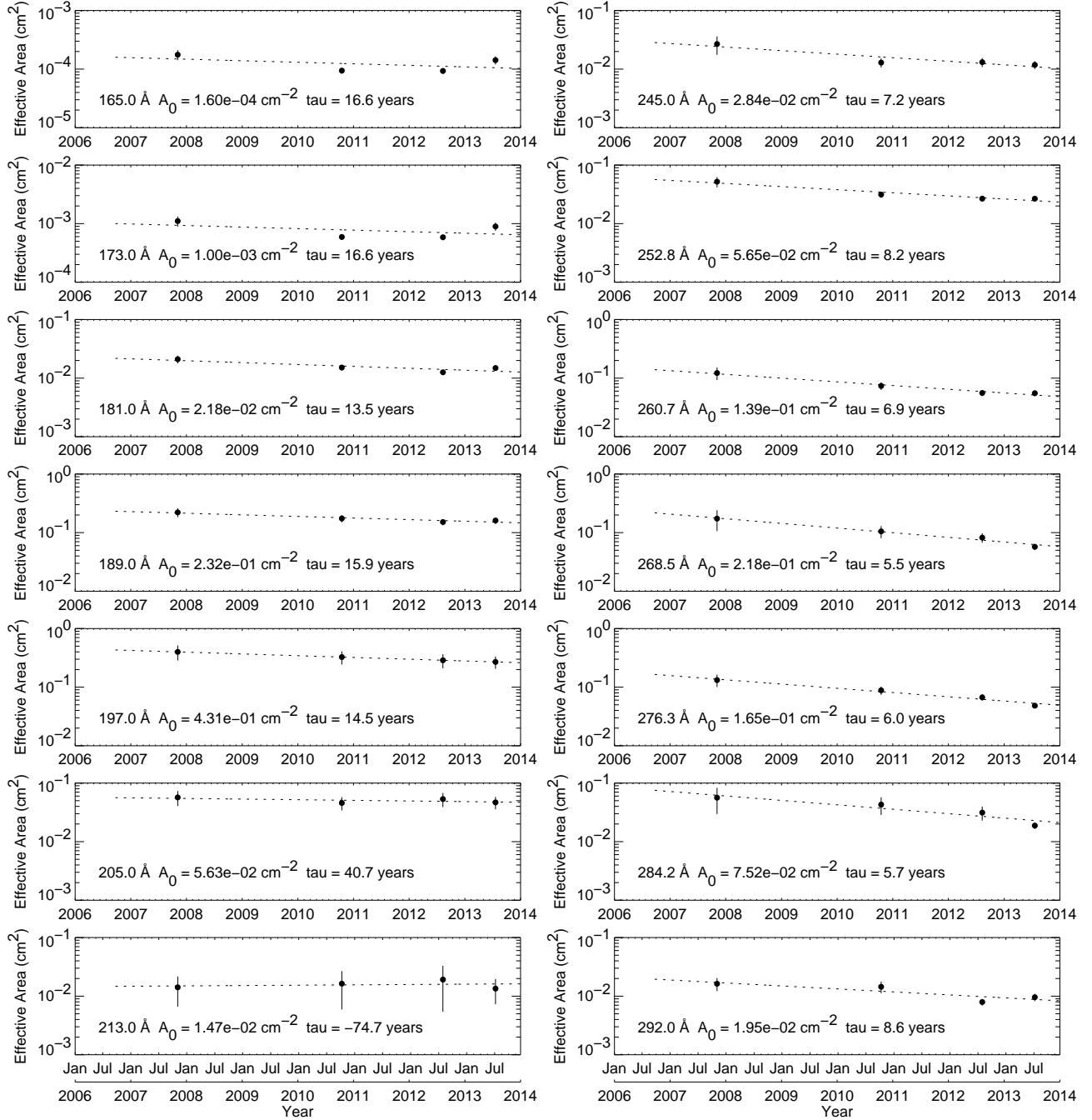


FIG. 5.— The evolution of the effective areas at the spline knots. Error bars derived from the least-squares fitting are shown. The dotted lines are exponential fits to the effective area as a function of time.

In this section we investigate the application of the time-dependent effective areas to various datasets that have been used to characterize the EIS calibration. We have written a routine that implements Equation 7 by evaluating the time constants at the wavelengths of the spline knots and interpolating to the wavelength of interest. We can then recalibrate an intensity derived from the pre-flight calibration using

$$I_{\text{corrected}}(\lambda, t) = I_{\text{pre_flight}}(\lambda) \frac{A_{\text{pre_flight}}(\lambda)}{A_{\text{corrected}}(\lambda, t)}. \quad (8)$$

In Figure 6 we show the intensities from the EIS synop-

tic program which periodically measures the intensities of selected emission lines in the quiet Sun. These data were analyzed by Mariska (2013). The revised effective area curves correct the observed secular declines in both the Fe VIII 185.213 Å and He II 256.317 Å lines. Our corrections, however, introduce a secular increase in the Si VII 275.368 Å. The origin of this increase is unclear.

The problems with EIS observations of the Fe XIV 274.203/211.316 Å ratio were noted first by Del Zanna (2013). As shown in Figure 7, the observed ratio, which should be approximately constant, decays exponentially dur-

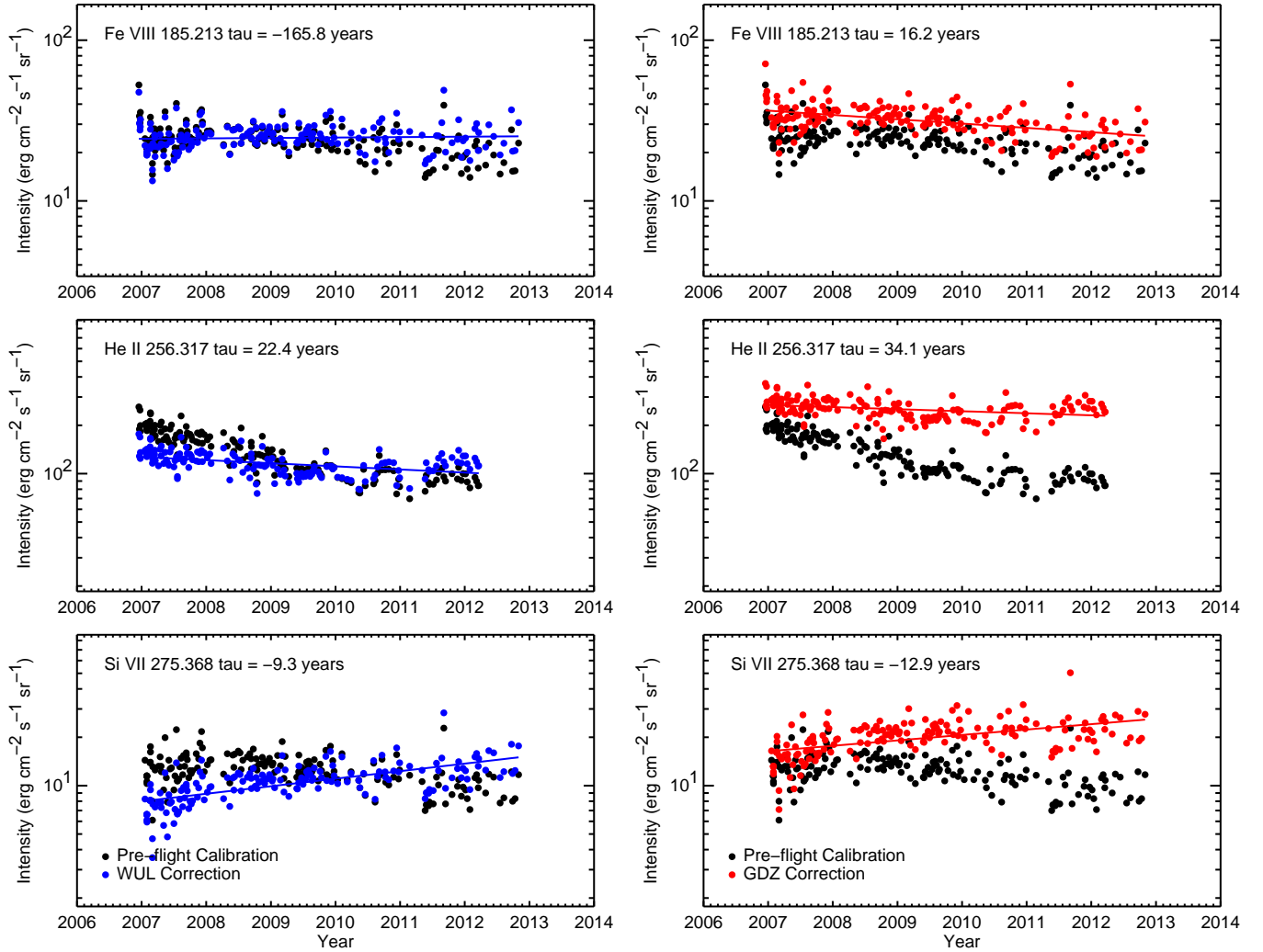


FIG. 6.— EIS synoptic observations re-calibrated using the effective areas derived in this paper as well as those from Del Zanna (2013). These data are from Mariska (2013). The new effective area curves can account for the secular declines in the He II 256.317 Å and Fe VIII 185.213 Å intensities, but overcorrect Si VII 275.368 Å.

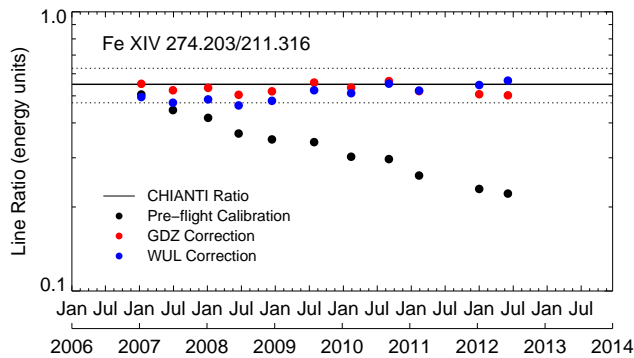


FIG. 7.— The evolution of the EIS Fe XIV 274.203/211.316 Å ratio as a function of time. These measurements are taken from active region observations. The solid line represents the theoretical value. The dotted lines represent the uncertainties in the theoretical ratio assuming a statistical uncertainty of 10% for each intensity measurement.

ing the *Hinode* mission. The corrected effective areas derived from our analysis account for much of the deviation from the theoretical value. Note that our analysis suggests that the change in the ratio is due to a combination of a decrease in sensitivity at 274 Å and a slight increase in sensitivity at 211 Å. The corrections suggested by Del Zanna (2013) are even closer to theory. These corrections account for the change in the ratio using only a decrease in the sensitivity at 274 Å.

Young et al. (2013) and Del Zanna (2013) noted that the Fe XXIV 192.04/255.10 Å ratio also disagreed with theory. In Figure 8 we show observed ratios for these lines derived from several observations taken over the past several years. The line ratio observed with EIS is typically about 4, much different than the well established theoretical ratio of 2.49 (in energy units).

Recently EIS has observed a large flare above the limb using an autonomous observing mode. These observations provide relatively high spatial resolution rasters during much of the event and extensive measurements of the Fe XXIV line

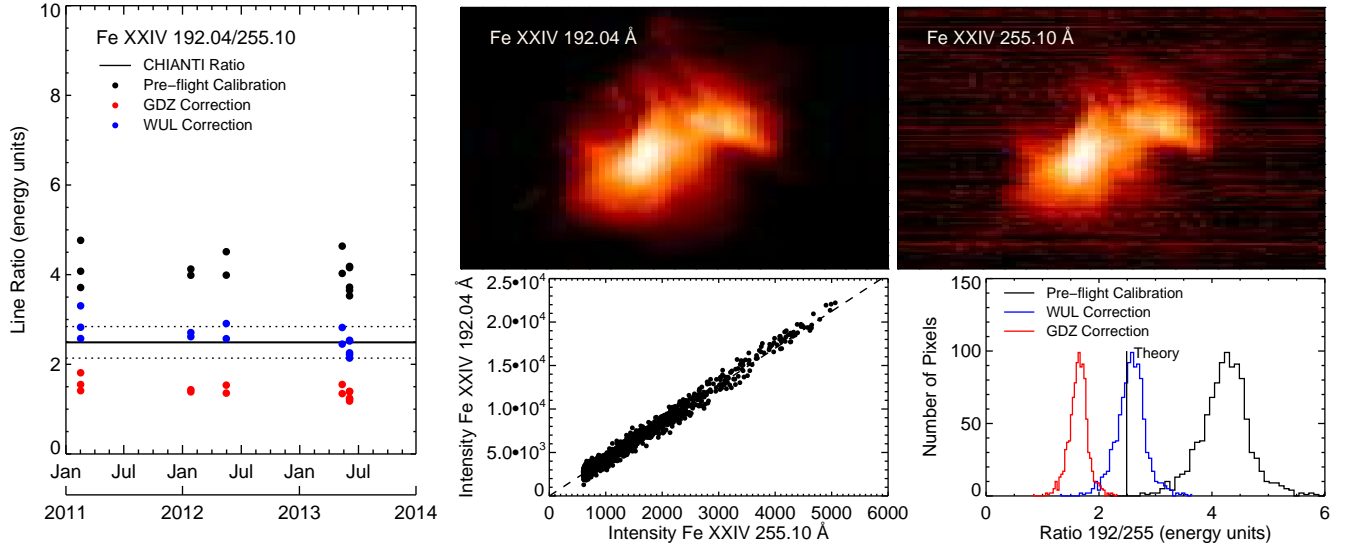


FIG. 8.— Observed and corrected Fe XXIV 192.04/255.10 Å ratios as a function of time. For a temperature of 10 MK the theoretical ratio is approximately 2.49 in energy units. Recent observations are close to 4.5 and show considerable scatter. The left panels show ratios derived from several spot checks of flare observations. The right panels show more systematic observations from a new observing sequence that provides higher spatial resolution. These data from an M5.9 flare that was observed by EIS on 2013 June 7. These rasters are from a scan that began at about 23:13 UT. The scatter plot shows the intensities for each line as well as a constant ratio of 4.24, which the median value for these observations. Only intensities above a threshold in the 255 Å line are used. The histograms show the distributions of observed and corrected ratios. The corrected effective areas derived from our analysis bring the observations into good agreement with theory.

ratio. The analysis of these observations indicate that the corrected effective areas derived from our analysis can bring the observed ratio into agreement with theory. The corrections suggested by Del Zanna (2013) overcorrect the ratio somewhat.

Early in 2013 Fe XIV 211.316 Å and 274.203 Å were added to the EIS full-disk mosaic program. As indicated in Table 1, for the Fe XIV 211.316 Å mosaics we find an EIS/EVE ratio of about 1.5. This is consistent with our finding that the pre-flight effective areas at this wavelength are too small. We measure an EIS/EVE irradiance ratio of 0.55 for Fe XIV 274.203 Å. Again, this is consistent with our finding that the effective area at this wavelength is currently below the pre-flight value. Similarly, the EIS/EVE irradiance ratios for Fe IX 180.401 Å, Fe XIII 202.044 Å, He II 256.317 Å, and Fe XV 284.160 Å are all consistent with the general trends in the effective areas derived from our analysis. We note, however, that the time constants derived from the EIS/EVE irradiance ratios are not always consistent with those derived from our DEM analysis. For example, the DEM analysis suggests a time constant of 10.2 years near 180 Å while the EIS/EVE ratio indicates 18.0 years.

5. SUMMARY AND DISCUSSION

We have presented an analysis of the absolute calibration of the EIS instrument on *Hinode*. This analysis, which attempts to reconcile EIS observations with both EVE irradiance measurements and the atomic data for most of the available emission lines, confirms that the changes to the EIS calibration are a complex function of both time and wavelength as found by Del Zanna (2013).

The corrections proposed here can account for many of the problems with the use of the pre-flight EIS calibration, such as the changes in the Fe XIV 274.203/211.316 Å and Fe XXIV 255.10/192.04 Å line ratios. Ultimately, however, we find that

it is not possible to fully reconcile all of the observations. Some of the time constants inferred from the EIS/EVE ratios, for example, are different than those inferred from the DEM analysis. It seems likely that the wavelength-dependent corrections to the EVE observations are not yet fully understood, but this is unlikely to resolve all of the differences that we have found. The corrections that we propose to the effective areas imply a secular increase in the Si VII 275.368 Å quiet Sun intensities. The origin of this is unclear. One possibility is that we have not fully accounted for the inhomogeneity in the evolution of the effective area.

As is illustrated in Figure 9, there is good agreement between our results and the corrections suggested by Del Zanna (2013) at many wavelengths. There are, however, three primary differences: 1) We extrapolate the exponential decay observed in the EIS-EVE ratio back to the beginning of the *Hinode* mission, which suggests higher effective areas at launch. 2) We find that the effective area above about 200 Å is higher than the pre-flight value by as much as 50%. 3) Our values for the effective areas in the long wavelength channel are generally about 50% higher than those given by Del Zanna (2013). The extrapolation of the EIS-EVE trend is difficult to justify. It does, however, successfully account for the evolution of the Fe VIII 185.213 Å quiet Sun intensities (see Figure 6). Also, as indicated in Table 1, EIS irradiances at 211 Å implied by the pre-flight calibration are about 1.52 times those observed with EVE while EIS irradiances at 275 Å are about 0.54 times those observed with EVE. Both values are approximately consistent with the effective areas we have derived through our analysis. At other wavelengths, however, the EIS-EVE ratios are not consistent with our analysis. These lines are generally strongly blended in EVE and these ratios are more difficult to interpret. More extensive analysis is required to resolve these issues.

We also cannot reconcile our analysis of the EIS calibra-

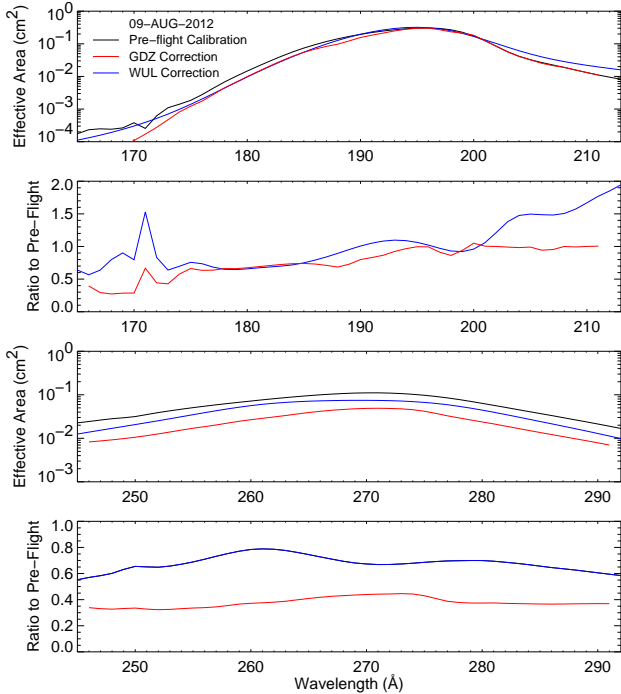


FIG. 9.— A comparison of the EIS effective areas determined from the pre-flight calibration, Del Zanna (2013), and this work (WUL). Both the absolute effective areas and the ratios of the revised effective areas to the pre-flight values are shown. These curves are for 2012 August 9, a period for which there is good agreement among all three sets of effective areas near 195 Å.

tion with the EIS-EUNIS inter-calibration. Wang et al. (2011) found a ratio of EIS to EUNIS of approximately 1.22. This ratio was independent of wavelength, suggesting that the shape of the EIS pre-flight effective areas were correct but that the instrumental sensitivity had decayed somewhat since launch. However, if we adjust the EIS intensities found in Table 4 of their paper based on the corrections that we have derived here, the ratio of EUNIS to EIS jumps to approximately 2 for many wavelengths. Since we tied the absolute EIS calibration to EVE this implies that the EUNIS absolute calibration is not consistent with that of EVE. EUNIS was flown again on 2013 April 23 so we will have an opportunity to revisit this issue.

The time constants for changes in the EIS calibration that we find are generally long relative to the length of the mission. While this implies that the calibration is changing relatively slowly, it does amplify the uncertainties in the revised effective areas. The sparsity of the available data also significantly limits our ability to discern more complicated patterns in the evolution of the instrumental sensitivity. For example, it is possible that the sensitivity has decayed at different rates at different times during the mission, but our analysis cannot account for this.

We have written software routines that return both pre-flight and modified effective area curves for a given wavelength and observing time. These routines have been incorporated into the SolarSoftware distribution of the standard EIS analysis software. One strategy for working with EIS observations is to continue using the pre-flight calibration during the initial data processing and then correct the intensities to account for new effective areas. This would allow for different corrections to be considered.

Given the complex nature of the changes to the calibra-

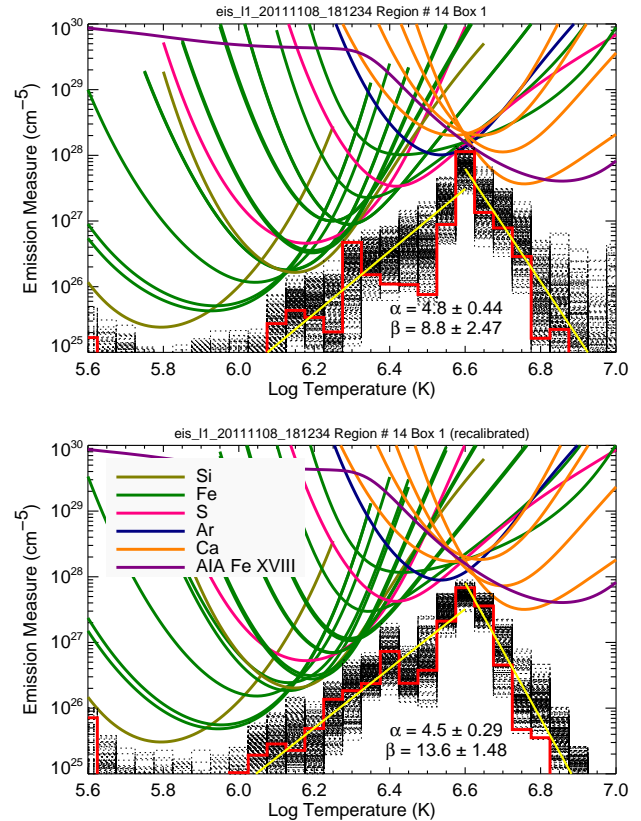


FIG. 10.— Active region differential emission measure curves derived using the pre-flight (top panel) and corrected effective areas (bottom panel). The emission measure distribution is the red curve. The black curves are solutions that use perturbed intensities. The general features of the emission measure distribution are largely unchanged.

tion it is difficult to assess their impact on previous analysis. Any analysis that is based on a only few lines is likely to be the most sensitive to any changes in the effective areas and should be reconsidered. In contrast, any analysis that involves many lines is likely to remain largely unchanged. To illustrate this we have recomputed the active region differential emission measures from Warren et al. (2012) using our new effective area curves. In all cases the re-calibrated intensities yield emission measure distributions that are similar to those derived using the pre-flight calibration. Example DEMs are shown in Figure 10 and the corresponding intensities are given in Table 3. We note that the inversions computed with the revised calibration generally have a χ^2 that is about a factor of 2 smaller than those computed with the pre-flight values for the effective areas.

The presence of time and wavelength dependent changes to the EIS calibration indicate that comprehensive synoptic observations are an important component of sensitivity monitoring. Simply measuring several wavelengths in the quiet Sun is insufficient. Our analysis suggests that routine monitoring of the quiet corona above the limb could be useful for identifying relative changes to the effective area of spectroscopic instruments over time. Since such an analysis is likely to require very deep exposures it would need to be implemented as part of a special observing campaign. Ultimately, however, new techniques need to be developed that provide simple yet accurate measurements of sensitivity over time.

TABLE 3
AN EXAMPLE RE-ANALYSIS OF ACTIVE REGION OBSERVATIONS^a

| Line | Pre-flight | | | Corrected | | |
|-----------------|------------|-----------|-----|-----------|-----------|-----|
| | I_{obs} | I_{dem} | R | I_{obs} | I_{dem} | R |
| Si VII 275.368 | 8.8 | 8.4 | 1.0 | 11.2 | 12.0 | 0.9 |
| Fe IX 188.497 | 10.5 | 11.5 | 0.9 | 10.8 | 11.7 | 0.9 |
| Fe IX 197.862 | 8.0 | 7.6 | 1.1 | 8.1 | 7.9 | 1.0 |
| Fe X 184.536 | 56.5 | 40.8 | 1.4 | 73.1 | 48.6 | 1.5 |
| Fe XI 180.401 | 279.7 | 255.4 | 1.1 | 398.8 | 309.4 | 1.3 |
| Fe XI 188.216 | 139.5 | 124.5 | 1.1 | 146.6 | 150.0 | 1.0 |
| S X 264.233 | 21.1 | 21.4 | 1.0 | 24.5 | 23.3 | 1.1 |
| Si X 258.375 | 55.0 | 79.3 | 0.7 | 65.4 | 87.4 | 0.7 |
| Fe XII 192.394 | 128.1 | 122.1 | 1.0 | 111.7 | 129.3 | 0.9 |
| Fe XII 195.119 | 433.1 | 377.4 | 1.1 | 388.2 | 399.8 | 1.0 |
| Fe XIII 202.044 | 576.9 | 331.6 | 1.7 | 456.4 | 362.7 | 1.3 |
| Fe XIII 203.826 | 657.9 | 381.2 | 1.7 | 438.2 | 347.5 | 1.3 |
| Fe XIV 264.787 | 330.4 | 376.7 | 0.9 | 388.3 | 391.8 | 1.0 |
| Fe XIV 270.519 | 185.6 | 210.5 | 0.9 | 241.7 | 226.0 | 1.1 |
| Fe XV 284.160 | 4921.1 | 6169.3 | 0.8 | 6481.2 | 6575.5 | 1.0 |
| S XIII 256.686 | 380.7 | 455.0 | 0.8 | 476.7 | 486.4 | 1.0 |
| Fe XVI 262.984 | 728.8 | 732.3 | 1.0 | 832.2 | 684.3 | 1.2 |
| Ar XIV 194.396 | 50.7 | 53.4 | 0.9 | 44.5 | 48.6 | 0.9 |
| Ca XIV 193.874 | 282.7 | 197.8 | 1.4 | 245.8 | 174.5 | 1.4 |
| Ca XV 200.972 | 247.3 | 170.3 | 1.5 | 225.5 | 144.2 | 1.6 |
| Ca XVI 208.604 | 127.1 | 107.9 | 1.2 | 82.1 | 87.2 | 0.9 |
| Ca XVII 192.858 | 110.8 | 138.6 | 0.8 | 96.0 | 104.6 | 0.9 |
| AIA 94 | 14.4 | 17.6 | 0.8 | 14.4 | 13.9 | 1.0 |

^a The observed intensities (I_{obs}) are from region #14 in Warren et al. (2012). Calculated intensities (I_{dem}) are from the an emission measure inversion. The variable R is I_{obs}/I_{dem} . EIS intensities are in units of $\text{erg cm}^{-2} \text{s}^{-1} \text{sr}^{-1}$. AIA intensities are in units of DN s^{-1} .

REFERENCES

- Boerner, P. F., Testa, P., Warren, H., Weber, M. A., & Schrijver, C. J. 2013, *Sol. Phys.*, submitted
- Culhane, J. L., et al. 2007, *Sol. Phys.*, 243, 19
- Del Zanna, G. 2013, *A&A*, 555, A47
- Delaboudinière, J.-P., et al. 1995, *Sol. Phys.*, 162, 291
- Dere, K. P., Landi, E., Mason, H. E., Monsignori Fossi, B. C., & Young, P. R. 1997, *A&AS*, 125, 149
- Feldman, U. 1992, *Phys. Scr*, 46, 202
- Feldman, U., Schühle, U., Widing, K. G., & Laming, J. M. 1998, *ApJ*, 505, 999
- Hock, R. A., Chamberlin, P. C., Woods, T. N., Crotser, D., Eparvier, F. G., Woodraska, D. L., & Woods, E. C. 2012, *Sol. Phys.*, 275, 145
- Korendyke, C. M., et al. 2006, *Appl. Opt.*, 45, 8674
- Landi, E., Feldman, U., & Dere, K. P. 2002, *ApJ*, 574, 495
- Landi, E., Young, P. R., Dere, K. P., Del Zanna, G., & Mason, H. E. 2013, *ApJ*, 763, 86
- Lang, J., et al. 2006, *Appl. Opt.*, 45, 8689
- Lemen, J. R., et al. 2012, *Sol. Phys.*, 275, 17
- Mariska, J. T. 2013, *Sol. Phys.*, 282, 629
- Markwardt, C. B. 2009, in *Astronomical Society of the Pacific Conference Series*, Vol. 411, *Astronomical Data Analysis Software and Systems XVIII*, ed. D. A. Bohlender, D. Durand, & P. Dowler, 251
- Raymond, J. C., et al. 1997, *Sol. Phys.*, 175, 645
- Tousey, R., Bartoe, J.-D. F., Brueckner, G. E., & Purcell, J. D. 1977, *Appl. Opt.*, 16, 870
- Wang, T., Thomas, R. J., Brosius, J. W., Young, P. R., Rabin, D. M., Davila, J. M., & Del Zanna, G. 2011, *ApJS*, 197, 32
- Warren, H. P., & Brooks, D. H. 2009, *ApJ*, 700, 762
- Warren, H. P., Winebarger, A. R., & Brooks, D. H. 2012, *ApJ*, 759, 141
- Woods, T. N., et al. 2012, *Sol. Phys.*, 275, 115
- Young, P. R., Doschek, G. A., Warren, H. P., & Hara, H. 2013, *ApJ*, 766, 127